tralateral axonal delays that establish the map of interaural delays. Thus, even if insufficient by themselves, a combination of the contralateral delays (triangles in upper right quadrant) and some of the ipsilateral delays (squares in the lower left quadrant) could sum to the needed physiological range of delays. The estimated delays are replotted versus CF in Figure 14*D*. For each fiber, the (extrapolated) delay at the rostral pole of the MSO is anchored to the horizontal line at 0 delay, and a vertical line is drawn to the extrapolated delay at the caudal pole. The line extends to positive delays for nearly all contralateral projections (triangles), and also for the four ipsilateral projections (squares) with negative slopes in Fig. 14*B*; these projections could all contribute to the pattern of interaural delays reported by Yin and Chan (1990). The individual data points show the estimated delays for individual endpoints, and the short horizontal bars delimit the range of delays of the linear regression over which endpoints are actually found. The gray rectangle approximates the range of physiological delays (400 μs) that is presumed to be represented in the MSO of one side. Again, the range of delays subserved by contralateral projections is small, but could suffice when combined with the ipsilateral delays.

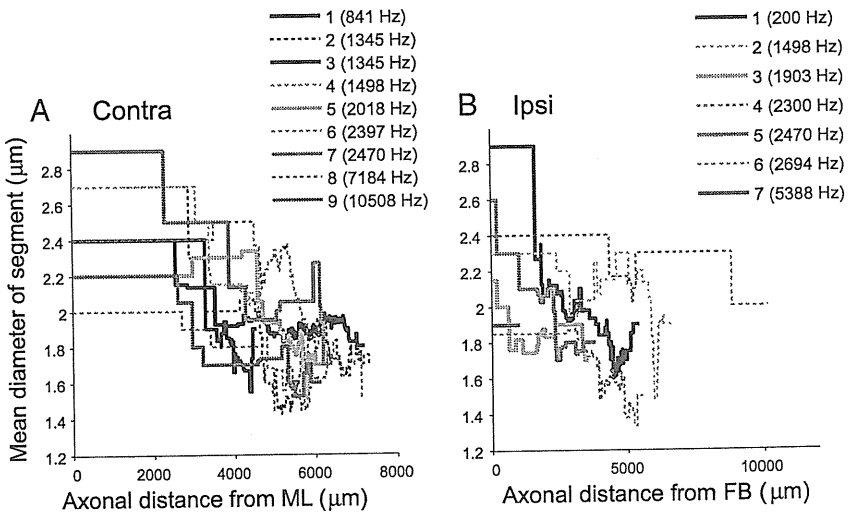

Figure 11. *A*, *B*, Average axon diameters decrease as a function of distance from the midline (*A*, Contra projections) or from the first branch point (*B*, Ipsi projections).

As was first reported in the guinea pig (McAlpine et al., 2001), the distribution of best delays in the inferior colliculus of the cat (Hancock and Delgutte, 2004; Joris et al., 2006) does not follow the shaded gray rectangle, but is largely restricted to the area defined by horizontal line at zero delay and the upper hyperbole at half a characteristic period (CF^{-1}), and this is also the case for recordings of the MSO in rodents (Brand et al., 2002; Pecka et al., 2008). Binaural recordings have shown that best delays have a specific distribution pattern that is constrained by the upper hyperbole and the horizontal. Taken at face value, the axonal delay estimates of the present results are not consistent with the pattern of binaural delays thought to be represented in the MSO. There is no suggestion in the distribution of estimated delays toward larger delays at low than at high CFs.

Figure 14 focuses on the ranges of estimated delay, taking as anchor points the midline (Fig. 14*A*), the first branch point (Fig. 14*B*), or the rostral pole (Fig. 14*D*). The inherent longer path length of contralateral projections combined with the similarity of axon diameter in contralateral and ipsilateral projections (Fig. 12) implies a systematic additional delay for the contralateral inputs. Comparison of the entire contralateral and ipsilateral delay generated by an axon is difficult because that would require backfilling of the soma and labeling of the entire projection to both contralateral and ipsilateral MSO. However, we can make an estimate of the difference in delay between contralateral and ipsilateral inputs. Taking into account that individual fibers project both contralaterally and ipsilaterally, and, assuming mirror symmetry between left and right sides of the brainstem, we only need to increase the contralateral delay estimates of Figure 14*A* (made with respect to the midline) with the delay estimated for the axonal segment between the ipsilateral first branch point and the midline [Fig. 15*B*, distance from ipsilateral first branchpoint (FBi) to midline]. We could trace this segment in all ipsilaterally projecting fibers. The average segment length was 4994 μm

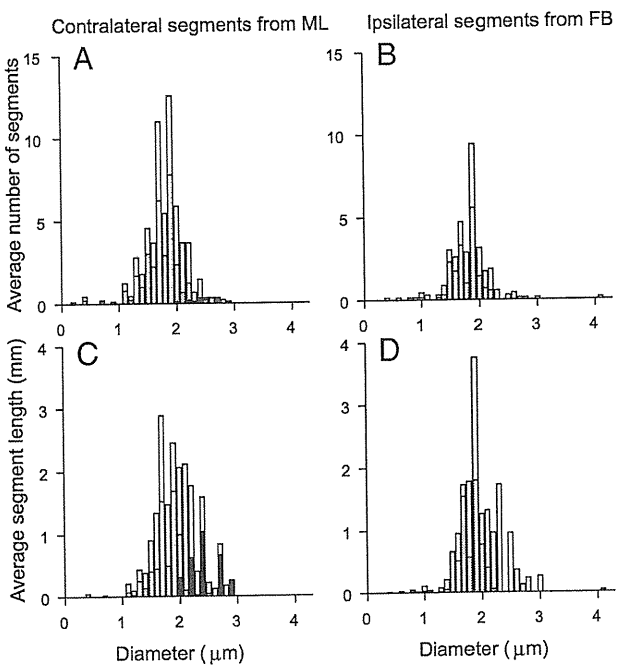

Figure 12. *A–D*, Distribution of axon diameters does not differ between contralateral (*A*, *C*) and ipsilateral (*B*, *D*) projections. The top histograms show the average number of segments with a given diameter (0.1 μm bins); the bottom histograms show the corresponding average length (in mm) at that diameter. All histograms are averages calculated for the entire population of contralateral and ipsilateral fibers, normalized to the total number of fibers included. The starting segments were ML (contralateral fibers) and FB (ipsilateral fibers). White bars include all the segments from starting segment to endpoints. Gray bars show length of most distal segments, terminated by endpoints. Black bars show length of most proximal segments, which contain ML (contralateral fibers only).

(range, 3748–6106 μm), and the average diameter was 2.6 μm (range, 1.9–3.0 μm), yielding an average extra delay (Eq. 1) of 221 μs (range, 139–351 μm). Thus, on average the endpoint delay estimates in Figure 14*A* would need to be increased by 221 μs. The value of 221 μs may be an overestimate because the axon diameters of our small sample seem to be an underestimate (Eq. 1); larger axon diameters at the midline were reported by Smith et al. (1993) (2.5–5 μm) and Brownell (1975) (3–5 μm).

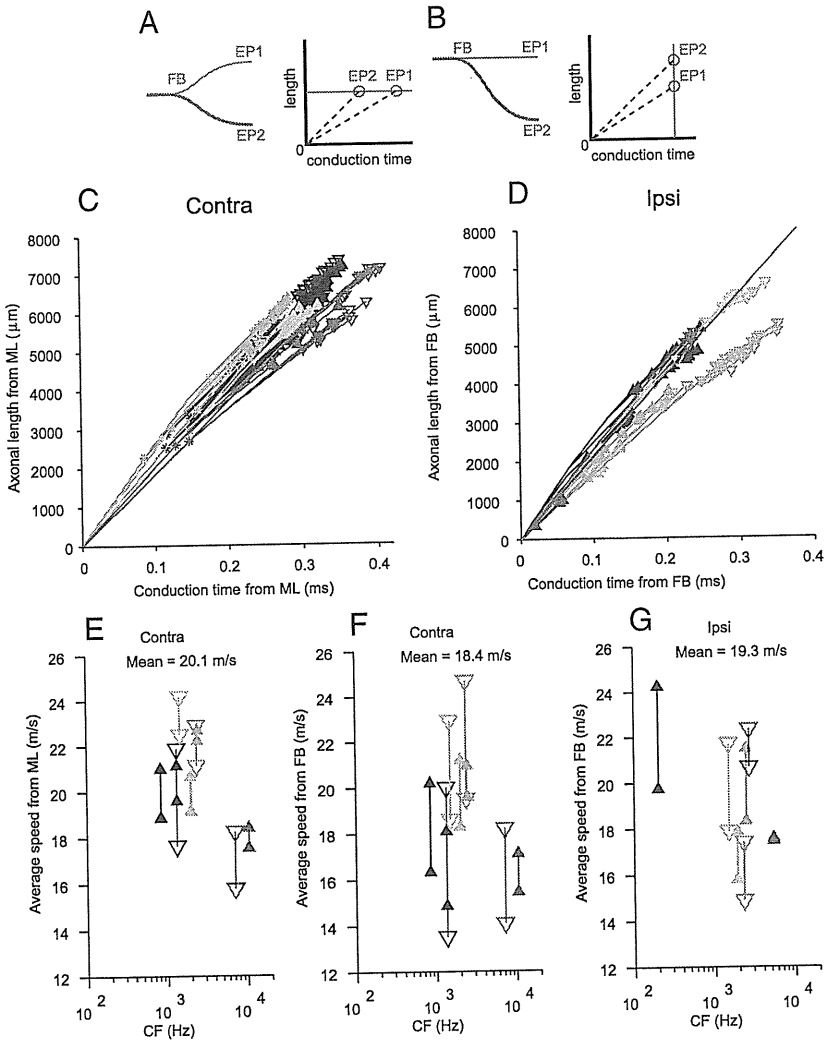

Figure 13. Axonal length is linearly related to estimated conduction time. Axonal lengths are measured as in Figures 7 and 11. Conduction time for each endpoint is the sum of conduction times of all segments leading up to that endpoint, calculated from segment length and diameter (see text). Diagrams in ***A*** and ***B*** illustrate configurations that would result in nonsloping relationships. ***C***, Length and time for contralateral projections, using ML as reference point. ***D***, Length and time for ipsilateral projections, using FB as reference point. One outlying endpoint is clipped off. ***E***, ***F***, Estimated average conduction speeds for all endpoints. This is the slope of the lines connecting the endpoints in ***C*** and ***D*** with the origin at (0,0), as illustrated with the dashed lines in ***A*** and ***B***. ***E–G***, Reference point at (0,0) was ML (***E***) or FB (***F***, ***G***). Color code and symbols are identical to Figures 8 and 10. The symbols indicate the lowest and highest speed for the endpoints of a given fiber.

The values of Beckius et al. (1999) (slightly >2 μm) are comparable to our own.

Note that inclusion of this extra delay does not alleviate the problem pointed out in Figure 14*D*, since it adds a constant delay common to all endpoints of a given fiber and does not increase the range of available delays provided by a given fiber. Figure 15*A* shows the estimated average (symbols) and range (lines) of path lengths from the last common axonal point (FBi) to all endpoints, as a function of CF, using the average of 4994 μm for the distance from FBi to midline calculated above. On average, the contralateral pathway from FBi onward is 10.78 mm, and the ipsilateral pathway is 4.21 mm. Incorporating the measured diameters, the average delay from the first ipsilateral branch point to MSO is an estimated 511 μs for the contralateral projections and 220 μs for the ipsilateral projections. Thus, the difference in path length is on average 6.57 mm, which generates an extra delay for the contralateral projection of an estimated 290 μs. Notwithstanding the uncertainty of its exact value, this extra delay must contribute to the contralateral bias of best delays seen in all studies of the MSO and inferior colliculus. It is interesting to observe that this value is similar to the ~200 μs extra contralateral delay in the lateral superior olive, estimated with different physiological methods (Joris, 1996; Joris and Yin, 1998; Tollin and Yin, 2005).

Axonal delay in the dorsoventral dimension

Differences in the CF of contralateral and ipsilateral inputs converging on MSO neurons have been proposed as a source of internal delays (Schroeder, 1977; Shamma, 1989; Bonham and Lewis, 1999). Cross-correlation analysis of responses of auditory nerve fibers revealed that disparities of a fixed distance on the cochlear basilar membrane generate a wider range of internal delays at low than at high CFs, in accord with the pattern of internal delays inferred from recordings in the inferior colliculus (Joris et al., 2006). However, to explain not only the decrease in the range of best delays with CF, but also the decrease in mean best delay with CF, an additional mechanism is needed. Because most contralateral projections approach the MSO from a rostral and ventral position (Figs. 2*C*, 3*A*,*B*), it was hypothesized (Joris et al., 2006) that the longer distance toward the dorsal (low-CF) pole of the MSO compared with the ventral (high-CF) pole perhaps causes a systematically longer delay for low-CF than for high-CF contralateral inputs. This hypothesis is illustrated with the schematic in Figure 15*C*. In Figure 15*D*, we show the mean and SD of the axonal lengths from midline to endpoint for all contralateral projections as a function of fiber CF (for individual data points, see Fig. 13*C*). There is no hint of a CF dependency showing longer lengths for the most dorsally projecting fibers (lowest CFs). The low-CF (Fig. 15*E*) and high-CF (Fig. 15*F*) projections illustrated in coronal view show that the tilting of the dorsal edge of the MSO toward the midline, combined with the angling of the contralateral low-CF fibers, is such that indeed no differential delay would be expected relative to the more ventral, high-CF projections. There is therefore no evidence in our data for a length gradient along the dorsoventral dimension in the excitatory inputs from the contralateral ear.

Discussion

Sensitivity to temporal differences in the sounds to the two ears provide a powerful model system to study neural temporal processing. Putative axonal delay lines have been an important component of models and of theorizing regarding such processing (Jeffress, 1948; Licklider, 1959; McFadden, 1973; Carr and Konishi, 1988; Cariani, 2004). There is general agreement that sensi-

tivity to ITDs involves internal delays causing a temporal shift of inputs from one ear relative to the other. What is increasingly questioned is the proposal (Jeffress, 1948) of a conversion of a temporal code to a place code by virtue of axonal delay lines. We quantitatively reanalyzed projection patterns of spherical bushy cells of the AVCN to MSO (Smith et al., 1993). The main findings of that study hold up and are consistent with a later study (Beckius et al., 1999); axonal configurations that are qualitatively of the nature surmised by Jeffress (1948) are found for contralateral projections, and less clearly for ipsilateral projections. Nonetheless, these configurations are not consistent in a simple form with the binaural data that have become available since.

Previous studies

The two previous reports on anatomical delay lines in the cat have complementary virtues. The power of the data of Smith et al. (1993) is that their 18 axons were physiologically characterized and that the labeling was unambiguously from single fibers, but filling was incomplete so that, typically, projections on only one side could be reconstructed. Their report showed one contralateral and one ipsilateral computer reconstruction. Beckius et al. (1999) labeled a large number of axons by injecting the rostral pole of the AVCN, of which 17 well filled axons (from 2 animals) were quantitatively reconstructed, with 7 reported in detail. Disadvantages of that material are the absence of physiology and the difficulty in connecting pieces across sections. Both studies have few data at very low CFs, where the largest best delays are observed. Best frequencies at the site of injection in Beckius et al. (1999) were estimated at ~1.5–1.75 kHz, but the tonotopic layering of the projections suggests that the actual range of CFs was much larger. In Smith et al. (1993), only two fibers had CF <1 kHz.

Despite differences in technique, the two studies were consistent, finding caudally directed delay line patterns contralaterally and a complex, less systematic pattern ipsilaterally. Quantitative analysis allowed Beckius et al. (1999) to discern a weaker length gradient in ipsilateral branches, in a direction opposite to the contralateral pattern. The quantitative analysis presented here is largely consistent with that of Beckius et al. (1999). The main additional findings concern the ipsilateral projections. We found caudally directed delay lines in three (of seven)

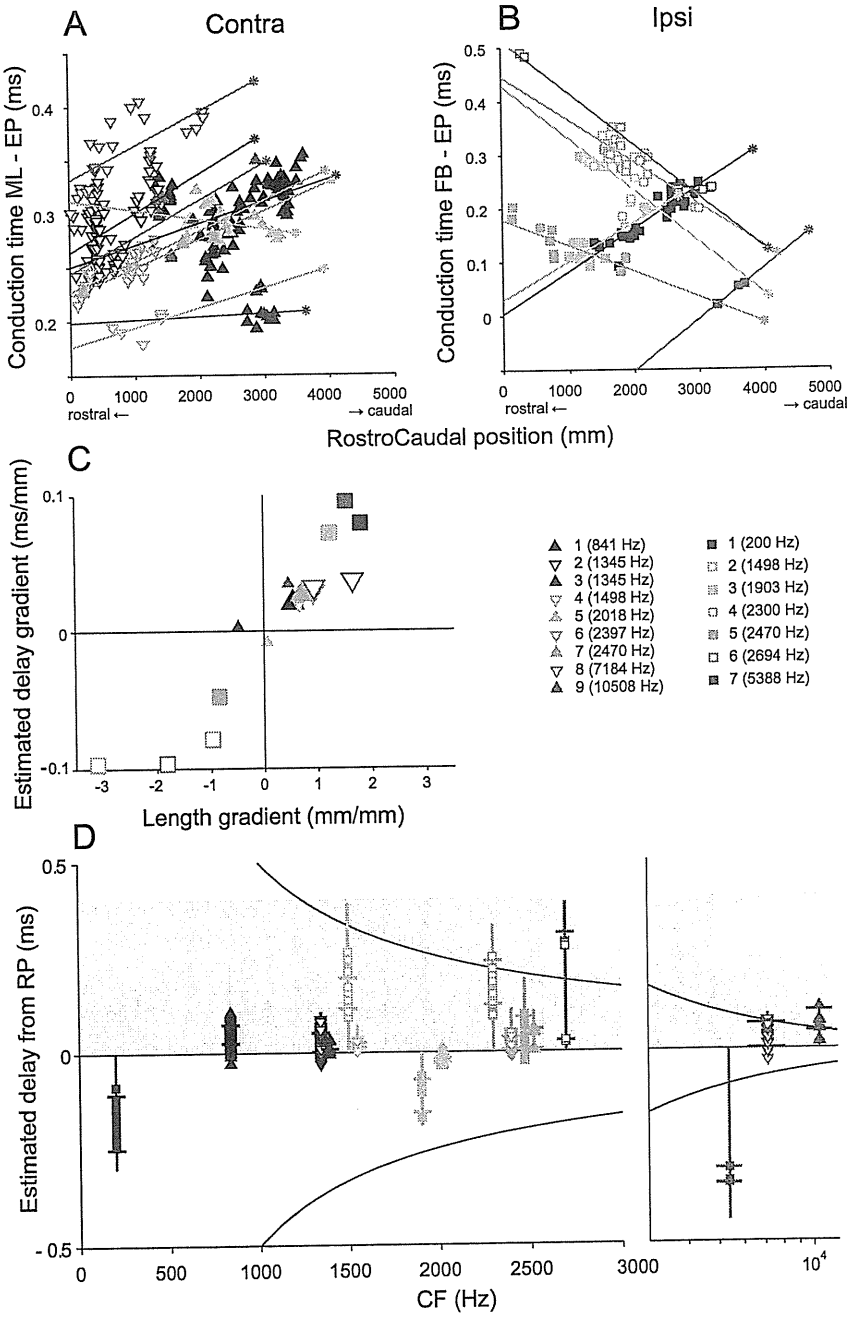

Figure 14. Rostrocaudal gradients of conduction time. ***A***, ***B***, Relationship between estimated conduction time and location of EP in rostrocaudal dimension in contralateral (***A***) and ipsilateral (***B***) fibers. The abscissa is zeroed to the position of the most rostral section in which MSO could be identified, and abscissa values are the distance of endpoints to that most rostral section. Ordinate values are the estimated conduction times from the midline (***A***, contralateral projections) or first branch point (***B***, ipsilateral projections). Solid lines are linear regressions. The asterisks at the end of each line indicate the most caudal MSO section. Note that the ordinate in ***B*** has a wider range than in ***A***. ***C***, Summary of regression slopes of Figure 8, *A* and *B* (abscissa), and of ***A*** and ***B*** (ordinate). Large symbols indicate values that are significant for both abscissa and ordinate. Contra 4 showed significance ($p < 0.05$) for length but not for delay; and vice versa for Contra 9. ***D***, Relationship between estimated delay and CF. The anchor point of each colored vertical line at 0 delay represents the RP of the MSO. The opposite end shows the extrapolated delay at the CP (corresponding to the delay accumulated between RP and the asterisk in ***A*** and ***B***). The small horizontal bars show the range of delays of the linear regression over which endpoints are present. Symbols and lines at positive delays, in the shaded region, are for fibers with a pattern consistent with the trend observed by Yin and Chan (1990); these are the fibers with positive slope in ***A*** or negative slope in ***B***. Symbols and lines at negative delays are for fibers with an opposite branching pattern (negative slope in ***A*** or positive slope in ***B***). Hyperbolic curves indicate the π limit (i.e., the extent of one period equaling CF^{-1}). The scale of the abscissa is linear in the left panel and logarithmic in the right panel.

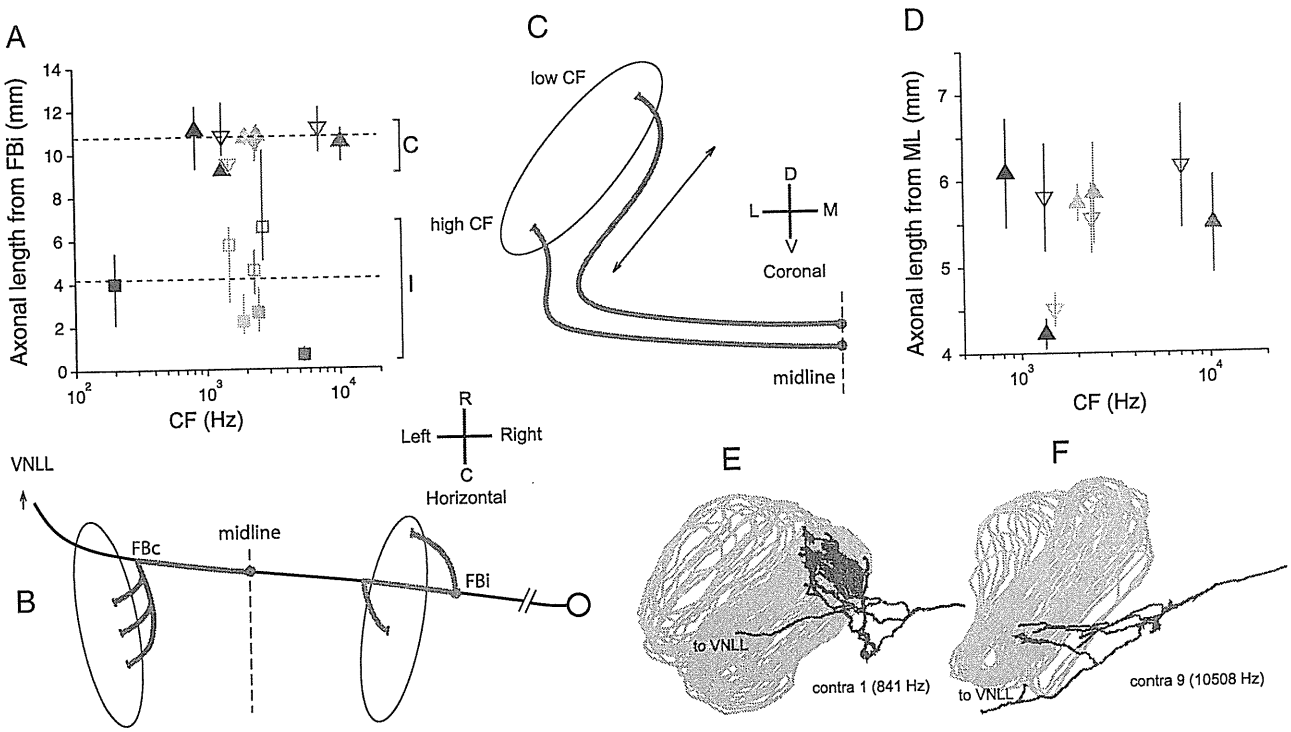

Figure 15. ***A, B***, Differences in path length between ipsilateral and contralateral inputs. ***A***, Estimated average and range of lengths for contralateral and ipsilateral projections between the FB of the ipsilateral MSO projection and the endpoints. Dashed lines show overall contralateral (C) and ipsilateral (I) mean. ***B***, Schematic of the measurement. The length of the trajectory between midline and contralateral endpoints (red), or between FBi and endpoints (green), was measured (same values as in Fig. 13*C,D*). To estimate the difference in length of contralateral and ipsilateral inputs, the red segment needs to be augmented by the distance FBi to midline: we use the average measured on ipsilateral projections (4994 μm, see main text). ***C–F***, Absence of length differences in the innervation from the contralateral ear along the dorsoventral dimension of MSO. ***C***, Hypothetical scheme of innervation by contralateral fibers, suggesting extra length for the most dorsally projecting (low-CF) fibers. If input fibers approach the MSO from ventral, low-CF fibers may have longer axonal length (arrow) to innervate the dorsal part of MSO than high-CF fibers for the ventral part. ***D***, relationship between axonal length from ML to endpoints, and CF. Symbols in ***A*** and ***D*** indicate average axonal length; lines are range (***A***) and SD (***D***) for each projection (symbol color and shape as in Fig. 8). ***E, F***, Coronal view of contralateral projections of fibers with lowest and highest CF (840 and 10,508 Hz, respectively).

ipsilateral reconstructions (i.e., where the length gradient was in the same direction as that of contralateral projections). This pattern was particularly convincing in the fiber with the lowest CF (200 Hz). Also, the rostrally directed delay line in the remaining four ipsilateral reconstructions was at least as steep (though of opposite sign) as that of the contralateral fibers (Figs. 8*B*, 14*C*), while in Beckius et al. (1999) the gradients on the ipsilateral side were shallow and constrained in rostrocaudal extent.

Anatomical patterns and best delays

Ultimately, "delay" is a functional concept requiring functional measurements. Particularly appealing in the morphological observations is their apparent consistency with the relationship between binaural tuning and cell location observed by Yin and Chan (1990), both in sign and in size. In that study, small best delays were found rostrally and large delays caudally, consistent with a caudally directed delay line contralaterally and/or a rostrally directed delay line ipsilaterally. Moreover, the range of physiological delays is reasonably in accord with estimated length differences and conduction speeds: a range of ~400 μs could be covered by combining "monaural" contralateral and ipsilateral delays.

Nevertheless, our quantitative analysis brings out several problems. Most importantly, there is nothing in the pattern of estimated delays observed that would suggest a CF-dependent range of delays (Fig. 14*D*). The anatomical branching patterns, as illustrated in Figures 2 and 3, are equally present at high and low CFs. In contrast, the physiological distribution of best delays measured in the MSO and inferior colliculus shows a clear dependence on CF, in cat and in other mammals studied (Brand et al., 2002; McAlpine and Grothe, 2003; Hancock and Delgutte, 2004; Joris et al., 2006; Pecka et al., 2008).

A second problem, of relevance beyond the issue of axonal delay lines, is that of correct concatenation. None of the afferents illustrated here or in Beckius et al. (1999) innervates the entire rostrocaudal extent of the MSO. Thus, each tonotopic strip of MSO neurons must be supplied by a patchwork of afferents. This complicates the structural basis for a systematic rostrocaudal gradient, since it requires correct temporal stacking of collaterals. For example, contralateral projections 2 and 3 have the same CF but innervate different portions of the MSO: projection 2 is to the rostral half and shows a positive slope, while projection 3 is restricted toward the caudal pole (Figs. 8*C*, 14*A*). Obviously, if these two fibers were representative for a single animal, the delay pattern generated by projection 2 would not be complemented by the inputs from projection 3. In other cases, fibers of similar CF appear to concatenate in an orderly manner (e.g., contralateral projections 5, 6, and 7). The fibers labeled here were derived from different animals, and offsets in the ordinate values of Figures 8, *C* and *D*, and 14, *A* and *B*, could reflect differences in anatomy between animals (e.g., in MSO size and location). Within-animal data are reasonably consistent in one animal studied by Beckius et al. (1999, their Fig. 11) but not in the other, which showed large offsets among fibers. However, the latter case also showed large variation in dorsoventral location of the projections, so that the labeled population must reflect a wide range of CFs. Together, the available material does not allow a prediction of the degree of

temporal dispersion that may be present across afferents of equal CF.

A third problem may be in the range of delays. The estimated contralateral delays are small relative to the values of best delay observed, particularly at low CFs where best delays can be >1 ms (Fig. 14, upper hyperbole) (Hancock and Delgutte, 2004; Joris et al., 2006). Ipsilateral delays tend to be larger than contralateral delays but are also more erratic in sign and rostrocaudal coverage. Combination of contralateral and ipsilateral delays can enlarge the net interaural delay (when the slopes are of opposite sign for the contralateral and ipsilateral projections), but sources of delay in addition to the delays provided by the within-fiber branching pattern are needed to account for the full range of best delays observed at low CFs. We caution that the diameter measured on our material is necessarily a rough estimate, as is the relationship between fiber diameter and conduction speed (Waxman and Bennett, 1972), and is suited for observing trends rather than absolute values.

Our reanalysis casts doubts on the relevance of the rostrocaudal axonal branching patterns for interaural delay, but does not by itself contradict the evidence for a spatial map of delay in MSO (Yin and Chan, 1990). Nevertheless, taking into account the noise in the relationship observed by Yin and Chan (1990), the absence of a clear relationship in multiunit recordings (Oliver et al., 2003), and the problems in tying the distribution of best delays to axonal branching patterns (Fig. 14*D*), it appears increasingly doubtful that these patterns are an essential component of the binaural circuit.

A final qualification is that other features of the branching pattern—different from the simple within-axon delay line configuration—may contribute to internal delay. For example, contralateral/ipsilateral asymmetries in temporal dispersion, in convergence across CFs, and in convergence ratio could all contribute to the pattern of best delays observed. Also, based on our material we cannot exclude that patches of contralateral and ipsilateral fibers would provide the range of best delays observed (for comparison, see Goldberg and Brown, 1969). It is interesting in this regard that there is more consistency in the pattern of projections to the rostral than to the caudal half of MSO (Fig. 8). Finally, there are other determinants of conduction speed, internodal distance in particular, which may show systematic variations in mammalian binaural circuits, as in birds (Carr and Konishi, 1990; Seidl et al., 2010).

Tonotopy: over- or under-representation of low frequencies?

A surprising finding is the tonotopic distribution of afferents. Their layering suggests that low frequencies are underrepresented rather than over-represented in the MSO. This is puzzling—functionally and anatomically—and is inconsistent with the "duplex" organization of the superior olivary complex (Irvine, 1986), comprising a low-frequency circuit computing ITD and a high-frequency circuit computing interaural level differences (ILDs). Taking the limited sample sizes of our data and those of Guinan et al. (1972) into account, a conservative statement is that MSO is tonotopically mapped isomorphic to the cochlea and has a low-frequency bias to the extent that very high CFs are not represented in MSO. The main duplex asymmetry is in the ILD (not the ITD) circuit: the lateral superior olive and medial nucleus of the trapezoid body show an apparent overrepresentation of high frequencies (Guinan et al., 1972).

References

Adams JC (1981) Heavy metal intensification of DAB-based HRP reaction product. J Histochem Cytochem 29:775.

Beckius GE, Batra R, Oliver DL (1999) Axons from anteroventral cochlear nucleus that terminate in medial superior olive of cat: observations related to delay lines. J Neurosci 19:3146–3161.

Bonham BH, Lewis ER (1999) Localization by interaural time difference (ITD): effects of interaural frequency mismatch. J Acoust Soc Am 106:281–290.

Brand A, Behrend O, Marquardt T, McAlpine D, Grothe B (2002) Precise inhibition is essential for microsecond interaural time difference coding. Nature 417:543–547.

Brownell WE (1975) Organization of the cat trapezoid body and the discharge characteristics of its fibers. Brain Res 94:413–433.

Cariani PA (2004) Temporal codes and computations for sensory representation and scene analysis. IEEE Trans Neural Netw 15:1100–1111.

Carr CE, Konishi M (1988) Axonal delay lines for time measurement in the owl's brainstem. Proc Natl Acad Sci U S A 85:8311–8315.

Carr CE, Konishi M (1990) A circuit for detection of interaural time differences in the brain stem of the barn owl. J Neurosci 10:3227–3246.

Goldberg JM, Brown PB (1969) Response of binaural neurons of dog superior olivary complex to dichotic tonal stimuli: some physiological mechanisms of sound localization. J Neurophysiol 22:613–636.

Greenwood DD (1990) A cochlear frequency-position function for several species 29 years later. J Acoust Soc Am 87:2592–2605.

Grothe B (2003) New roles for synaptic inhibition in sound localization. Nat Rev Neurosci 4:540–550.

Guinan JJ, Norris BE, Guinan SS (1972) Single auditory units in the superior olivary complex. II: locations of unit categories and tonotopic organization. Int J Neurosci 4:147–166.

Hancock KE, Delgutte B (2004) A physiologically based model of interaural time difference discrimination. J Neurosci 24:7110–7117.

Irvine DRF (1986) The auditory brainstem: a review of the structure and function of auditory brainstem processing mechanisms. Berlin: Springer.

Jeffress LA (1948) A place theory of sound localization. J Comp Physiol Psychol 41:35–39.

Joris P, Yin TC (2007) A matter of time: internal delays in binaural processing. Trends Neurosci 30:70–78.

Joris PX (1996) Envelope coding in the lateral superior olive. II. Characteristic delays and comparison with responses in the medial superior olive. J Neurophysiol 76:2137–2156.

Joris PX (2006) A dogged pursuit of coincidence. J Neurophysiol 96:969–972.

Joris PX, Yin TC (1998) Envelope coding in the lateral superior olive. III. Comparison with afferent pathways. J Neurophysiol 79:253–269.

Joris PX, Smith PH, Yin TC (1998) Coincidence detection in the auditory system: 50 years after Jeffress. Neuron 21:1235–1238.

Joris PX, Van de Sande B, Louage DH, van der Heijden M (2006) Binaural and cochlear disparities. Proc Natl Acad Sci U S A 103:12917–12922.

Liberman MC (1982) The cochlear frequency map for the cat: labeling auditory-nerve fibers of known characteristic frequency. J Acoust Soc Am 72:1441–1449.

Licklider JCR (1959) Three auditory theories. In: Psychology: a study of a science (Koch S, ed), pp 41–144. New York: McGraw-Hill.

McAlpine D (2005) Creating a sense of auditory space. J Physiol 566:21–28.

McAlpine D, Grothe B (2003) Sound localization and delay lines—do mammals fit the model? Trends Neurosci 26:347–350.

McAlpine D, Jiang D, Palmer AR (1996) Interaural delay sensitivity and the classification of low best-frequency binaural responses in the inferior colliculus of the guinea pig. Hear Res 97:136–152.

McAlpine D, Jiang D, Palmer AR (2001) A neural code for low-frequency sound localization in mammals. Nat Neurosci 4:396–401.

McFadden D (1973) Precedence effects and auditory cells with long characteristic delays. J Acoust Soc Am 54:528–530.

Oliver DL, Beckius GE, Bishop DC, Loftus WC, Batra R (2003) Topography of interaural temporal disparity coding in projections of medial superior olive to inferior colliculus. J Neurosci 23:7438–7449.

Palmer AR (2004) Reassessing mechanisms of low-frequency sound localisation. Curr Opin Neurobiol 14:457–460.

Palmer A, Kuwada S (2005) Binaural and spatial coding in the inferior colliculus. In: The inferior colliculus (Winer JA, Schreiner CE, eds), pp 377–410. New York: Springer.

Pecka M, Brand A, Behrend O, Grothe B (2008) Interaural time difference processing in the mammalian medial superior olive: the role of glycinergic inhibition. J Neurosci 28:6914–6925.

Rose JE, Gross NB, Geisler CD, Hind JE (1966) Some neural mechanisms in the inferior colliculus of the cat which may be relevant to localization of a sound source. J Neurophysiol 29:288–314.

Roth GL, Kochhar RK, Hind JE (1980) Interaural time differences: implications regarding the neurophysiology of sound localization. J Acoust Soc Am 68:1643–1651.

Schroeder MR (1977) New viewpoints in binaural interactions. In: Psychophysics and physiology of hearing (Evans EF, Wilson JP, eds), pp 455–467. New York: Academic.

Seidl AH, Rubel EW, Harris DM (2010) Mechanisms for adjusting interaural time differences to achieve binaural coincidence detection. J Neurosci 30:70–80.

Shamma SA, Shen NM, Gopalaswamy P (1989) Stereausis: binaural processing without neural delays. J Acoust Soc Am 86:989–1006.

Smith PH, Joris PX, Carney LH, Yin TC (1991) Projections of physiologically characterized globular bushy cell axons from the cochlear nucleus of the cat. J Comp Neurol 304:387–407.

Smith PH, Joris PX, Yin TC (1993) Projections of physiologically characterized spherical bushy cell axons from the cochlear nucleus of the cat: evidence for delay lines to the medial superior olive. J Comp Neurol 331:245–260.

Stotler WA (1953) An experimental study of the cells and connections of the superior olivary complex of the cat. J Comp Neurol 98:401–431.

Tollin DJ, Yin TC (2005) Interaural phase and level difference sensitivity in low-frequency neurons in the lateral superior olive. J Neurosci 25: 10648–10657.

Wagner H, Asadollahi A, Bremen P, Endler F, Vonderschen K, von Campenhausen M (2007) Distribution of interaural time difference in the barn owl's inferior colliculus in the low- and high-frequency ranges. J Neurosci 27:4191–4200.

Waxman SG, Bennett MV (1972) Relative conduction velocities of small myelinated and nonmyelinated fibers in the central nervous system. Nat New Biol 238:217–219.

Yin TC, Chan JC (1990) Interaural time sensitivity in medial superior olive of cat. J Neurophysiol 64:465–488.

Original Paper

ORL

ORL 2011;73:61–67
DOI: 10.1159/000323010

Received: July 20, 2010
Accepted after revision: November 23, 2010
Published online: January 5, 2011

Evaluation of the Carhart Effect in Congenital Middle Ear Malformation with Both an Intact External Ear Canal and a Mobile Stapes Footplate

Takashi Sakamoto[a] Akinobu Kakigi[a] Akinori Kashio[a] Kaori Kanaya[a]
Mitsuya Suzuki[b] Tatsuya Yamasoba[a]

[a]Department of Otolaryngology and Head and Neck Surgery, Graduate School of Medicine, Faculty of Medicine, University of Tokyo, Tokyo, and [b]Department of Otolaryngology and Head and Neck Surgery, Sakura Medical Center, University of Toho, Chiba, Japan

Key Words
Congenital middle ear malformation · Bone conduction threshold · Carhart effect · Mobile stapes footplate

Abstract
The medical charts of 41 ears with congenital middle ear malformation with both an intact external ear canal and a mobile stapes footplate were reviewed retrospectively to study the Carhart effect. The operations were categorized as successful or unsuccessful according to the extent of decrease in the average air-bone gap. Statistically significant differences were observed between the 2 groups with respect to the changes in pure-tone average and the changes in the bone conduction (BC) threshold at 1 and 2 kHz. Linear regression analysis revealed weak correlations between the change in the BC threshold and the postoperative BC threshold at an overall level and at the 4 frequencies tested. Stapes ankylosis is a main cause of the Carhart effect. The present study showed that in congenital middle ear malformation, the Carhart effect was caused not only by stapes ankylosis but also by other types of disruption in the ossicular chain.

Introduction

A middle ear abnormality causes a gap between the air and bone conduction (BC) thresholds and is often accompanied by a depression of the BC thresholds. This phenomenon was first reported by Carhart [1] in 1949. Later, he demonstrated an improvement in the BC threshold after successful fenestration surgery for otosclerosis, and this depression in the BC threshold was designated the Carhart notch. In the report, the depression was maximal at 2 kHz and ranged in frequency from 0.5 to 4 kHz. Therefore, it is suitable to designate the phenomenon Carhart effect instead of the Carhart notch [2].

The Carhart effect was also described in malleus fixation, otitis media with effusion, chronic otitis media, cholesteatoma, and congenital malformation of the middle ear [3–8]. The mechanism responsible for the Carhart effect is still not clearly understood, but it is attributed to a decrease in the external and middle ear components of BC transmission. In patients with a middle ear abnormality, it is difficult to distinguish whether the elevation of the BC threshold is true or false before surgery. If the BC thresholds are misunderstood, a surgeon may misjudge an indication for surgical intervention. Therefore, it is important to assess the Carhart effect in detail.

KARGER

Fax +41 61 306 12 34
E-Mail karger@karger.ch
www.karger.com

0301–1569/11/0732–0061$38.00/0

Accessible online at:
www.karger.com/orl

Takashi Sakamoto
Department of Otolaryngology and Head and Neck Surgery
Graduate School of Medicine, Faculty of Medicine, The University of Tokyo
Hongo 7-3-1, Bunkyo-ku, Tokyo 113-8655 (Japan)
Tel. +81 3 5800 8924, Fax +81 3 3814 9486, E-Mail tsakamoto-tky@umin.ac.jp

Congenital malformation of the middle ear is accompanied by various types of abnormalities in the middle ear, such as ossicular ankylosis, which includes a fixed stapes footplate, and disruption in the ossicular joint [9], but it is rarely accompanied by inflammatory lesions such as tympanosclerosis and the formation of granulation tissue. Therefore, congenital malformation of the middle ear with a mobile stapes footplate is an appropriate pathological lesion for evaluating the Carhart effect. It is well known that ankylosis of the stapes footplate causes the Carhart effect. However, to our knowledge, few reports have evaluated the Carhart effect in a series of patients with congenital malformation of the middle ear with a mobile stapes footplate. The present study aimed to evaluate differences in the change in BC thresholds at 0.5, 1, 2, and 4 kHz between successful and unsuccessful surgery groups. We also evaluated the correlations between the changes in the BC thresholds and the postoperative BC thresholds at an overall level and at the 4 frequencies by using linear regression analysis.

Materials and Methods

In this study, we examined 36 patients with congenital middle ear malformation with both an intact external ear canal and a mobile stapes footplate; 5 of these patients were affected bilaterally and 31 were affected unilaterally. Forty-one ears were operated by tympanoplasty at the Hospital of the University of Tokyo, and medical charts were retrospectively reviewed. This study was approved by the Ethics Committee of the University of Tokyo. All patients underwent a complete clinical examination, which included pure-tone audiometry, tympanometry with stapedial reflex, and a high-resolution temporal bone computed tomography. The diagnosis was confirmed in all cases during surgery. All patients included in the study had at least 1 year of follow-up.

Tympanoplasty was performed via the transcanal or retroauricular approach under general anesthesia. In tympanoplasty, the ossicular chain was reconstructed with autografts including the incus removed or tragal cartilage.

Pure-tone audiometry was conducted periodically (1 month after the operation and then every 2 months, for a minimum of 1 year after surgery). The preoperative and postoperative pure-tone average (PTA) values were calculated as the mean air conduction (AC) threshold at 0.5, 1, 2, and 4 kHz. The change in PTA was calculated as preoperative minus postoperative PTA. Cases whose average air-bone gap at 0.5, 1, 2, and 4 kHz decreased to within 20 dB were regarded as having a successful surgery, according to the guidelines of the Committee on Hearing and Equilibrium [10]. The ears operated were classified into successful and unsuccessful surgery groups. Congenital ossicular anomalies were divided into 5 categories according to the classification of Park and Choung [9]. In brief, type 1 includes patients with a normal stapes and an anomaly of the incus or malleus. Type 2 includes patients with a mobile footplate and other anomalies. Type 3 includes patients with stapes footplate fixation only. Type 4 includes patients with stapes footplate fixation and other anomalies. Type 5 includes patients with no stapes footplate and other anomalies. Types 1 and 2 were considered to have a mobile stapes footplate. Types 3, 4, and 5 were considered to have a fixed stapes footplate. Patients with types 1 and 2 disease were enrolled in the present study.

The change in the BC threshold was calculated as preoperative minus postoperative BC threshold at 0.5, 1, 2, and 4 kHz in pure-tone audiometry.

Differences in the preoperative PTA, the postoperative PTA, the change in the PTA and the BC threshold at 0.5, 1, 2, and 4 kHz between the successful and unsuccessful surgery groups were analyzed by using the Mann-Whitney test. Differences between the preoperative and postoperative BC thresholds at 0.5, 1, 2, and 4 kHz in each group were analyzed by using the Wilcoxon test. A p value of <0.05 was considered statistically significant.

We also evaluated the correlations between the change in the BC threshold and the postoperative BC threshold at an overall level and at the 4 tested frequencies by using linear regression analysis. Pearson's correlation coefficients between the 2 parameters were calculated.

Table 1. Demographic data of the successful and unsuccessful surgery groups

	Successful surgery group	Unsuccessful surgery group
Number of ears	23	18
Mean age at operation ± SD years	28.5 ± 20.1	17.6 ± 10.8
Sex (male/female)	12/11	9/9
Side of operation (right/left)	7/16	7/11
Type 1 malformation (ears)	20	14
Type 2 malformation (ears)	3	4

The 2 groups did not differ in terms of age at operation, sex, side of the operation, and the distribution of types of ossicular malformation.

Results

Table 1 presents the demographic data of the patients. In the successful surgery group, patients were aged 27.8 ± 20.0 years (mean ± SD). In the unsuccessful surgery group, patients were aged 21.8 ± 14.0 years (mean ± SD). The successful and unsuccessful surgery groups included 31 and 18 ears, respectively. Of the 23 ears in the successful surgery group, 12 were of male patients and 11 were of female patients, and 7 were right ears and 16 were left ears. Of the 18 ears in the unsuccessful surgery group, 9 were of male patients and 9 were of female patients, and 7 were right ears and 11 were left ears.

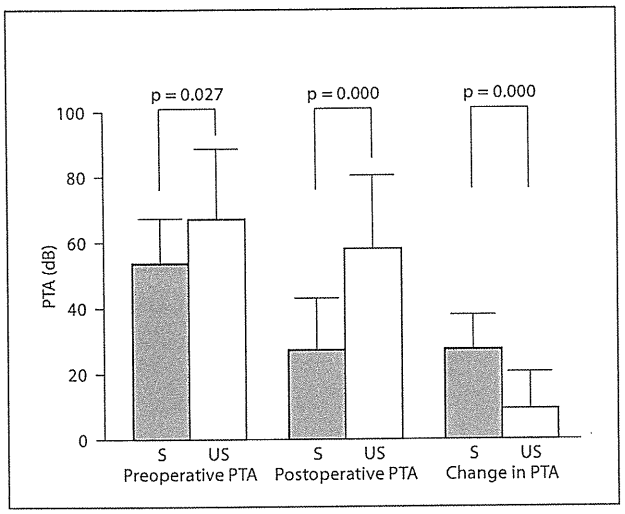

Fig. 1. The preoperative PTAs in the successful and unsuccessful surgery groups were 53.8 ± 14.5 and 66.9 ± 22.6 dB HL (mean ± SD), respectively. The p value revealed by the Mann-Whitney test for preoperative PTA was 0.027. The postoperative PTAs in the successful and unsuccessful surgery groups were 26.9 ± 16.0 and 57.8 ± 22.5 dB HL (mean ± SD), respectively. The p value revealed by the Mann-Whitney test for postoperative PTA was 0.000. The changes in PTA in the successful and unsuccessful surgery groups were 27.0 ± 10.6 and 9.1 ± 11.6 dB HL (mean ± SD), respectively. The p value revealed by the Mann-Whitney test for the difference in postoperative PTA was 0.000. Statistically significant differences in the preoperative and postoperative PTAs, and the changes in PTA between the successful and unsuccessful surgery groups were detected. S = Successful surgery group; US = unsuccessful surgery group.

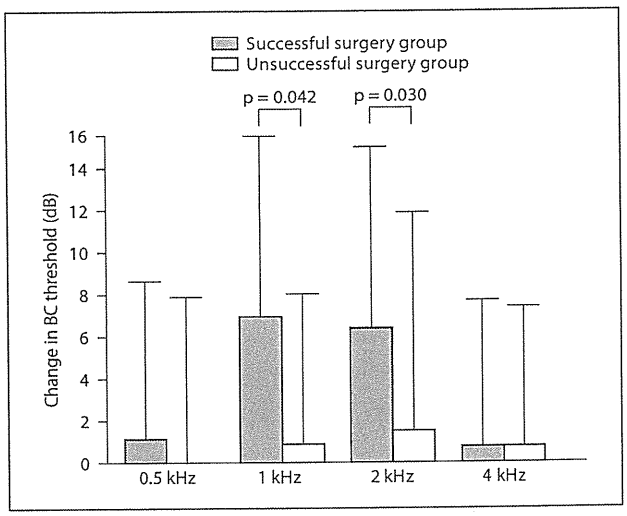

Fig. 2. In the successful surgery group, the changes in BC threshold at 0.5, 1, 2, and 4 kHz were 1.1 ± 7.6, 7.1 ± 8.8, 6.5 ± 8.9, and 1.1 ± 7.2 dB HL (mean ± SD), respectively. In the unsuccessful surgery group, the changes in BC threshold at 0.5, 1, 2, and 4 kHz were 0.0 ± 8.0, 0.83 ± 7.3, 1.5 ± 10.6, and 1.1 ± 6.8 dB HL (mean ± SD), respectively. The p values revealed by the Mann-Whitney test for the change in BC thresholds at 0.5, 1, 2, and 4 kHz were 0.378, 0.042, 0.030, and 0.915, respectively. Statistically significant differences for the change in BC threshold between the successful and unsuccessful surgery groups were identified at 1 and 2 kHz.

In the successful surgery group, type 1 and 2 anomalies included 20 and 3 ears, respectively. In the unsuccessful surgery group, type 1 and 2 anomalies included 14 and 4 ears, respectively.

The preoperative PTAs in the successful and unsuccessful surgery groups were 53.8 ± 14.5 and 66.9 ± 22.6 dB HL (mean ± SD), respectively. The p value for the Mann-Whitney test for preoperative PTA was 0.027 (fig. 1). Statistically significant differences in preoperative PTA between the successful and unsuccessful surgery groups were found.

The postoperative PTAs in the successful and unsuccessful surgery groups were 26.9 ± 16.0 and 57.8 ± 22.5 dB HL (mean ± SD), respectively. The p value revealed by the Mann-Whitney test for the difference in postoperative PTA was 0.000 (fig. 1). A statistically significant difference in postoperative PTA between the successful and unsuccessful surgery groups was found.

The changes of PTA in the successful and unsuccessful surgery groups were 27.0 ± 10.6 and 9.1 ± 11.6 dB HL (mean ± SD), respectively. The p value revealed by the Mann-Whitney test for the difference in postoperative PTA was 0.000 (fig. 1). The changes in PTA differed significantly between the successful and unsuccessful surgery groups.

In the successful surgery group, the preoperative BC thresholds at 0.5, 1, 2, and 4 kHz were 13.5 ± 11.7, 16.5 ± 15.1, 23.8 ± 17.6, and 18.0 ± 15.5 dB HL (mean ± SD), respectively. The postoperative BC thresholds at 0.5, 1, 2, and 4 kHz were 12.6 ± 11.9, 9.5 ± 12.8, 17.3 ± 17.1, and 17.0 ± 14.5 dB HL (mean ± SD), respectively. The p values revealed by the Wilcoxon test for differences between preoperative and postoperative BC thresholds at 0.5, 1, 2, and 4 kHz were 0.507, 0.002, 0.004, and 0.453, respectively. Statistically significant differences were found at 1 and 2 kHz.

In the unsuccessful surgery group, the preoperative BC thresholds at 0.5, 1, 2, and 4 kHz were 18.6 ± 17.4, 23.1 ± 20.7, 30.4 ± 20.2, and 26.3 ± 20.0 dB HL (mean ± SD), respectively. The postoperative BC thresholds at

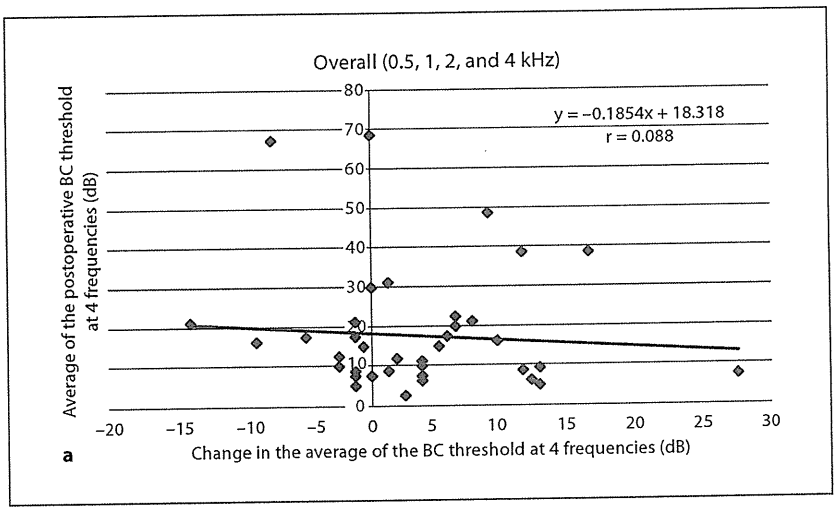

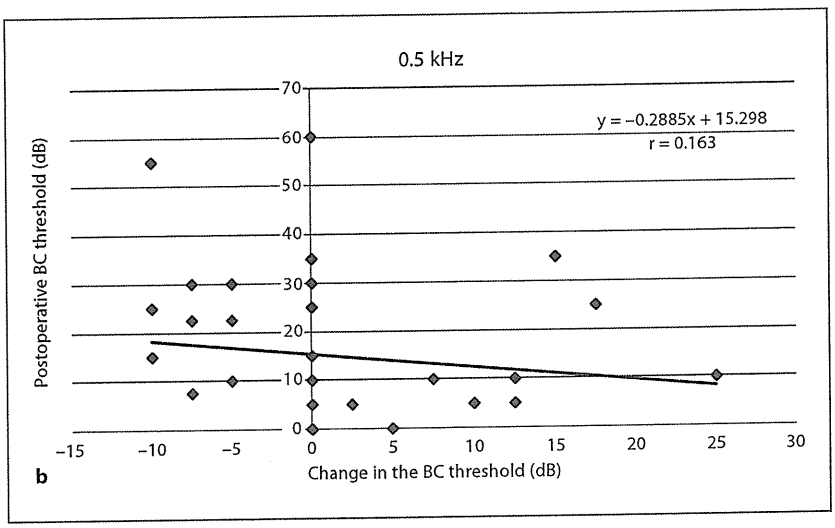

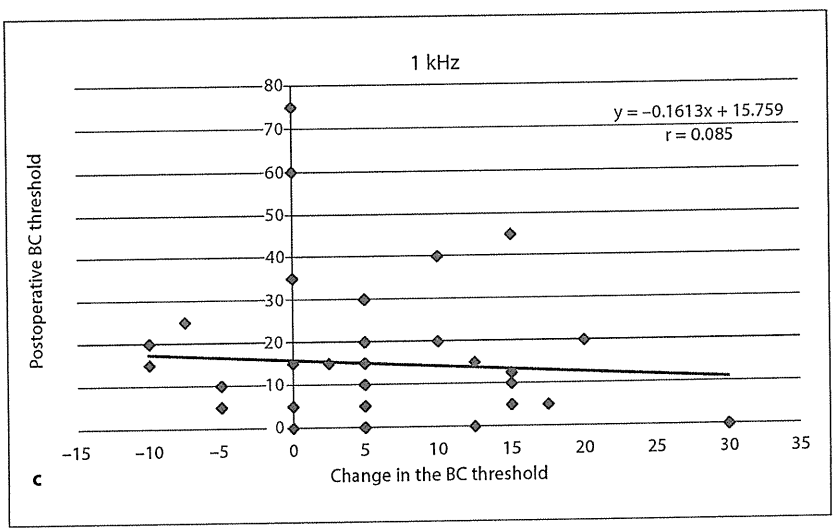

Fig. 3. a Linear regression analysis revealed weak correlations between the changes in the average BC threshold at 0.5, 1, 2, and 4 kHz and the average postoperative BC thresholds at the 4 frequencies. Pearson's correlation coefficient was 0.088. **b–e** Linear regression analysis revealed a weak correlation between the change in the BC threshold and the postoperative BC threshold at the 4 frequencies (**b**: 0.5 kHz, **c**: 1 kHz, **d**: 2 kHz, **e**: 4 kHz). Pearson's correlation coefficients at 0.5, 1, 2, and 4 kHz were 0.163, 0.085, 0.167, and 0.157, respectively.

0.5, 1, 2, and 4 kHz were 19.2 ± 15.0, 22.2 ± 18.0, 28.9 ± 17.2, and 23.8 ± 20.5 dB HL (mean ± SD), respectively. The p values revealed by the Wilcoxon test for differences between preoperative and postoperative BC thresholds at 0.5, 1, 2, and 4 kHz were 0.380, 0.750, 0.968, and 0.418, respectively. No statistically significant differences were found at any frequency.

In the successful surgery group, the changes in BC thresholds at 0.5, 1, 2, and 4 kHz were 1.1 ± 7.6, 7.1 ± 8.8, 6.5 ± 8.9, and 1.1 ± 7.2 dB HL (mean ± SD), respectively. In the unsuccessful surgery group, the changes in BC thresholds at 0.5, 1, 2, and 4 kHz were 0.0 ± 8.0, 0.83 ± 7.3, 1.5 ± 10.6, and 1.1 ± 6.8 dB HL (mean ± SD), respectively. The p values revealed by the Mann-Whitney test for the change in BC thresholds at 0.5, 1, 2 and 4 kHz were 0.378, 0.042, 0.030, and 0.915, respectively. Statistically significant differences for the change in the BC threshold between the successful and unsuccessful surgery groups were found at 1 and 2 kHz (fig. 2).

In linear regression analysis, Pearson's correlation coefficients at the overall level and at 0.5, 1, 2, and 4 kHz were 0.088, 0.161, 0.085, 0.167, and 0.157, respectively. The corresponding adjusted coefficients of determination (R^2) were −0.018 and 0.001, −0.018, 0.003, and 0.000. Linear regression analysis revealed positive but weak correlations between the changes in the BC threshold and the postoperative BC threshold at the overall level and at the 4 frequencies (fig. 3a–e).

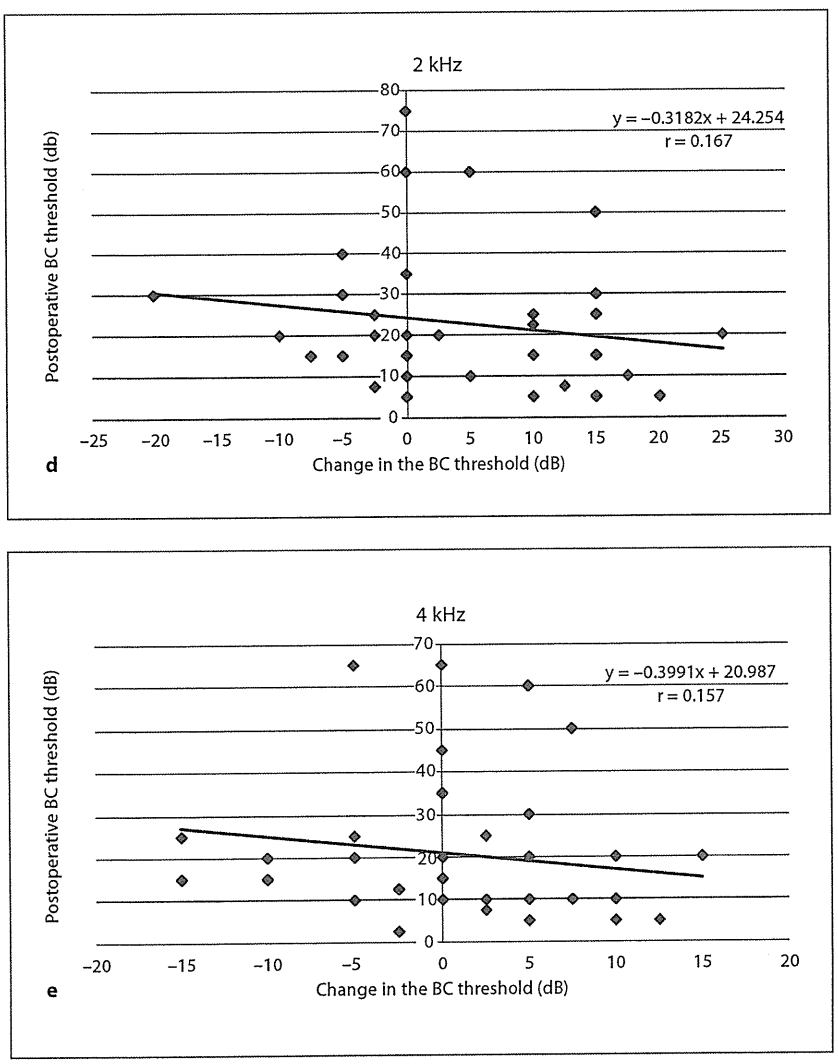

3

Discussion

In the present study, the Carhart effect in the successful surgery group was greater than that in the unsuccessful surgery group at 0.5, 1, and 2 kHz. However, statistically significant differences in the Carhart effect between the successful and unsuccessful surgery groups were identified at 1 and 2 kHz, and the Carhart effect at 1 kHz was slightly greater than that at 2 kHz. This study is the first to evaluate the Carhart effect in a series of patients having isolated congenital ossicular anomalies with a mobile stapes footplate.

The BC response employs 3 different modes: the compressional, inertial, and osseotympanic modes [11]. In the compressional mode, skull vibration caused by sound directly causes vibration of the otic capsule. In the inertial mode, skull vibration caused by sound induces movement in the ossicular chain due to the inertial force of the ossicles. In the osseotympanic mode, sound energy causes vibration of the skull and para-auditory structures (i.e. jaw and soft tissue), and these vibrations are transmitted from the external auditory canal to the ossicles through the tympanic membrane [12]. The disruption of the ossicular chain may prevent the effect of the inertial and osseotympanic modes, and this is thought to be the main cause of the Carhart effect.

In Carhart's classic report, the maximal elevation of the BC threshold was observed at 2 kHz and the elevation of BC was described in the range of frequencies from 0.5 to 4 kHz [2]. The range of frequencies in which the Carhart effect exists is controversial. Variations in the Carhart notch ranging from 0.5 to 4 kHz were reported in patients with otosclerosis [13]. Ginsberg et al. [14] reported that the effect in a large series of patients who underwent stapedectomy was approximately equal in frequencies between 0.5 and 2 kHz (15–18 dB). Cook et al. [15] reported that in 102 patients who underwent stapedectomy, linear regression analysis revealed significant linear relationships between the gain in the AC threshold and the gain in the BC threshold at 0.5, 1, 2, and 4 kHz, concluding that the Carhart effect was most prominent at 2 kHz, because the gradient of the regression line was steepest at 2 kHz.

The Carhart effect has also been described in malleus fixation, otitis media with effusion, chronic otitis media, and congenital malformation of the middle ear [3–8]. In contrast to otosclerosis, there are few reports that assess the Carhart effect in a large series of patients with congenital ossiclular anomalies. Isolated congenital ossicular anomalies can affect the ossicular chain in a wide range of modes, including ossicular ankylosis and disruption in the ossicular joint [9]. Therefore, reconstruction surgery for this condition is not as simple as that when done for otosclerosis and may involve a variety of operations from tympanoplasty to the release of ossicular ankylosis.

Yasan [16] assessed the change in the BC threshold after tympanoplasty for otosclerosis, tympanosclerosis, chronic otitis media, and a few cases of congenital ossicular anomalies and reported that the Carhart notch at 2 kHz indicated stapes footplate fixation, but that the Carhart notch at 1 kHz indicated a mobile stapes footplate. Their results disagree with our results because in the present study, the Carhart effect was observed at both 1 and 2 kHz in anomalies with a mobile footplate. Lee et al. [6] reported that the BC thresholds at 0.5, 1, 2, and 4 kHz were significantly improved after tympanoplasty for chronic otitis media, and the greatest improvement was observed at 2 kHz. In contrast, in the present study, a significant improvement in the BC threshold was identified at both 1 and 2 kHz, and the improvement at 1 kHz was slightly greater than that at 2 kHz. Moreover, the Carhart effect was not observed at 0.5 and 4 kHz. These results are inconsistent with the results of Lee et al. One possible explanation for the discrepancy between their results and ours is a difference in inclusion criteria. In the inclusion criteria of Lee et al., successful surgery was defined as an improvement in the mean of the AC threshold of 15 dB or more. In our inclusion criteria, however, successful surgery was defined as a decrease in the average air-bone gap at 0.5, 1, 2, and 4 kHz to within 20 dB according to the guidelines of the Committee on Hearing and Equilibrium [10]. The criteria of Lee et al. ensure that a real improvement has occurred after surgery, while our criteria generally ensure that the middle ear component is as near normal as possible. In our study, the change in PTA in the successful surgery group was significantly greater than that in the unsuccessful surgery group. This result demonstrates that our criteria properly reflect a real improvement in hearing and suggest that our criteria may be more stringent than the criteria of Lee et al.

Inclusion criteria are necessary for this kind of analysis. Unless appropriate inclusion criteria are applied, an analysis may lead to an underestimation of the Carhart effect [17].

In the present study, a significant improvement in the BC threshold was not identified at 4 kHz. The reason remains unsolved, but the deterioration of the BC threshold due to inner ear damage by surgery may be involved.

One possible explanation for the nonsignificance of the improvement in the BC threshold at 0.5 kHz is the occlusion effect of the external ear canal. In the open ear

canal, the sound pressure generated by BC is smaller than the threshold level. Sound pressure in the external ear canal caused by BC stimuli is elevated below 1 kHz when the external ear canal is occluded; this is called the occlusion effect [18–21] and is estimated to be up to 20 dB [22]. There remains the possibility that our result at 0.5 kHz was influenced by an underestimation of the Carhart effect because of the occlusion effect.

Moreover, surgical interventions cannot completely restore normal transmission of sound energy from the tympanic membrane to the oval window, and thus, postoperative BC thresholds may still include a residual Carhart effect. Hence, any method using preoperative and postoperative BC threshold is liable to underestimate the magnitude of the Carhart effect.

In the present study, linear regression analysis revealed positive but weak correlations between the changes in the BC threshold and the postoperative BC threshold at the overall level and at the 4 frequencies, although the significant Carhart notch was noted only at 1 and 2 kHz in the Mann-Whitney test. This discrepancy may be attributed to the difference in the methodology of statistical analysis. A relatively small sample size does not affect the statistical power of the nonparametric Mann-Whitney test. In contrast, to retain the statistical power, a larger sample size is required for linear regression analysis than for the Mann-Whitney test. Sample size in the present study was unlikely to be large enough for linear regression analysis to show a large correlation coefficient.

It is important to note that one should understand the true BC thresholds before ear surgery for congenital middle ear malformation with both an intact external ear canal and a mobile stapes footplate. Otherwise patients may miss an opportunity to have their hearing restored because surgeons may dismiss the idea of surgery due to a poor functional result.

In summary, the present study found that the Carhart effect was statistically significant at 1 and 2 kHz, and that the Carhart effect was slightly greater at 1 kHz than at 2 kHz. However, the occlusion effect may have caused the Carhart effect at 0.5 kHz to be underestimated. These results suggest that the deterioration of the BC threshold in congenital middle ear malformation with an intact external ear canal is caused not only by stapes ankylosis, but also by other kinds of disruption in the ossicular chain, and that the Carhart effect was identified at at least 2 frequencies even in the absence of a fixed stapes footplate.

Acknowledgement

The authors wish to thank Dr. Hitoshi Iwamura for his cooperation in data collection and statistical analysis.

References

1 Carhart R, Hayes C: Clinical reliability of bone conduction audiometry. Laryngoscope 1949;59:1084–1101.
2 Carhart R: Clinical application of bone conduction audiometry. Arch Otolaryngol 1950; 51:798–808.
3 Ahmad I, Pahor AL: Carhart's notch: a finding in otitis media with effusion. Int J Pediatr Otorhinolaryngol 2002;64:165–170.
4 Austin DF: Sound conduction of the diseased ear. J Laryngol Otol 1978;92:367–393.
5 Conijn EA, Van der Drift JF, Brocaar MP, Van Zanten GA: Conductive hearing loss assessment in children with otitis media with effusion. A comparison of pure tone and bera results. Clin Otolaryngol Allied Sci 1989;14: 115–120.
6 Lee HS, Hong SD, Hong SH, Cho YS, Chung WH: Ossicular chain reconstruction improves bone conduction threshold in chronic otitis media. J Laryngol Otol 2008;122: 351–356.
7 Moon CN Jr, Hahn MJ: Primary malleus fixation: diagnosis and treatment. Laryngoscope 1981;91:1298–1307.
8 Tuz M, Dogru H, Uygur K, Gedikli O: Improvement in bone conduction threshold after tympanoplasty. Otolaryngol Head Neck Surg 2000;123:775–778.
9 Park K, Choung YH: Isolated congenital ossicular anomalies. Acta Otolaryngol 2009; 129:419–422.
10 Committee on hearing and equilibrium guidelines for the evaluation of results of treatment of conductive hearing loss. American Academy of Otolaryngology-Head and Neck Surgery Foundation, Inc. Otolaryngol Head Neck Surg 1995;113:186–187.
11 Tonndorf J: A new concept of bone conduction. Arch Otolaryngol 1968;87:595–600.
12 Tsai V, Ostroff J, Korman M, Chen JM: Bone-conduction hearing and the occlusion effect in otosclerosis and normal controls. Otol Neurotol 2005;26:1138–1142.
13 Perez R, de Almeida J, Nedzelski JM, Chen JM: Variations in the 'Carhart notch' and overclosure after laser-assisted stapedotomy in otosclerosis. Otol Neurotol 2009;30:1033–1036.
14 Ginsberg IA, Hoffman SR, Stinziano GD, White TP: Stapedectomy – In-depth analysis of 2,405 cases. Laryngoscope 1978;88:1999–2016.
15 Cook JA, Krishnan S, Fagan PA: Quantifying the Carhart effect in otosclerosis. Clin Otolaryngol Allied Sci 1995;20:258–261.
16 Yasan H: Predictive role of Carhart's notch in pre-operative assessment for middle-ear surgery. J Laryngol Otol 2007;121:219–221.
17 Gatehouse S, Browning GG: A re-examination of the Carhart effect. Br J Audiol 1982; 16:215–220.
18 Huizing EH: Bone conduction-the influence of the middle ear. Acta Otolaryngol Suppl 1960;155:1–99.
19 Khanna SM, Tonndorf J, Queller JE: Mechanical parameters of hearing by bone conduction. J Acoust Soc Am 1976;60:139–154.
20 Stenfelt S, Wild T, Hato N, Goode RL: Factors contributing to bone conduction: the outer ear. J Acoust Soc Am 2003;113:902–913.
21 Tonndorf J: Bone conduction. Studies in experimental animals. Acta Otolaryngol 1966;Suppl 213:1+.
22 Stenfelt S, Goode RL: Bone-conducted sound: physiological and clinical aspects. Otol Neurotol 2005;26:1245–1261.

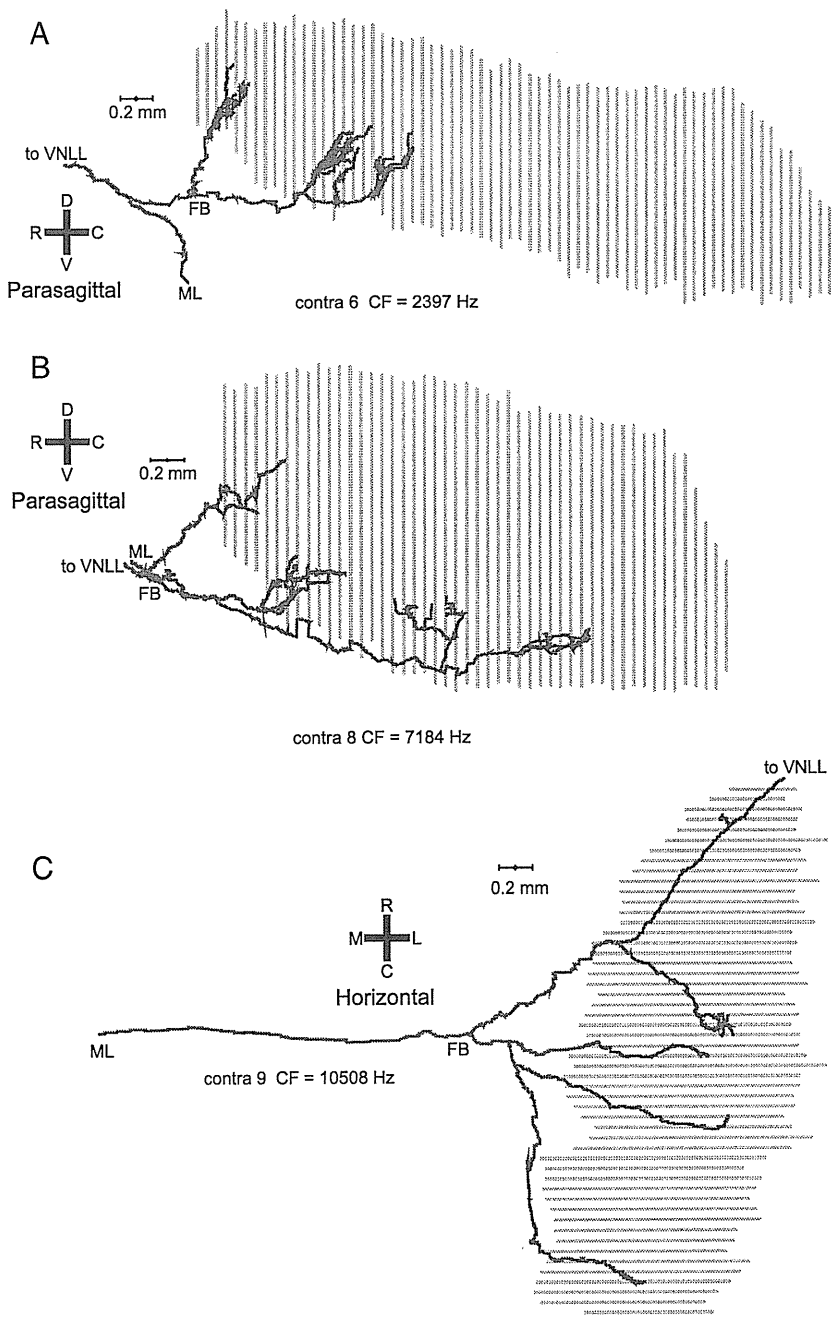

Figure 3. Delay line configuration in 3 contralaterally projecting fibers. ***A***, ***B***, Projections on a parasagittal plane. ***C***, Projection on a horizontal plane. CFs are indicated. Branches that end within the MSO are indicated in red.

that is directed rostrally and does not seem to fit the caudally directed delay line patterns of the fibers discussed so far. A similar case is shown in parasagittal view in Figure 4*A*. The axon also crosses the midline at a rostrocaudal position that bisects the MSO in approximately equal halves. It shows a number of caudally directed collateral branches with increasing length, but also a branch that innervates the rostral half of the MSO and continues on toward the VNLL. Fibers that reach the MSO at an even more caudal position are shown in Figure 4, *B* and *C*. The fiber in Fig. 4*B* has a rostrocaudally restricted field. The axon in Fig. 4*C* shows no obvious bias toward increasing length for more caudally projecting collaterals.

Ipsilateral projections

Seven ipsilaterally injected fibers were adequately labeled for our analyses. Because the pattern of the ipsilateral projections is more complicated than that of the contralateral projections described above, we show the projections in different views. The fiber illustrated in Figure 5 had several collaterals without an obvious delay line pattern. Two types of collateral projections can be distinguished: forward and backward. The coronal view (Fig. 5*A*) shows one branch coursing along the lateral aspect of the MSO (forward innervation), consistent with the known segregation of ipsilateral and contralateral inputs to the lateral and medial dendrites of MSO neurons, respectively (Stotler, 1953). Two more collaterals only branch off from the main axon after it has crossed underneath the MSO, to then loop back through the MSO to innervate the same region (backward innervation). These branches have their origins medial to the ipsilateral MSO. All of the seven ipsilateral projections had "backward" components; four of the seven ipsilateral projections had "forward" components (Fig. 10*B*, summary).

Figure 6 shows another example of an ipsilateral projection. In this case, the forward and backward innervation contribute endpoints that are located at different rostrocaudal positions (Fig. 6*B*,*C*), where the backward branches innervate a more rostral part of the MSO than the forward branches. The horizontal and parasagittal views suggest that this fiber has greater length in its caudal than in its rostral innervation, but the complex course of the branches in the three dimensions precludes a simple visual assessment. In fact, length measurements reveal greater length in the rostral than in the caudal innervation (see Fig. 8*D*, green inverted triangles).

Dendrograms

Because branches often extensively overlap in the projections of the computer reconstructions in Figures 1–6, these views do not give an adequate representation of the complexity of branching. Figure 7 gives an overview, for the most completely filled fibers, of the sequence of branchings in contralateral (left column) and ipsilateral (right column) projections. The horizontal axis indicates the length of segments bordered by midline, branch points, or endpoints. The vertical axis only serves to offset the different segments after branching: it does not have the physical meaning of length, and there is no vertical sorting according to position in the MSO. The dendrograms therefore provide information about branch sequence and length (abscissa), but they contain no anatomical directional information (e.g., lateral vs medial, dorsal vs ventral, rostral vs caudal). There is obviously profuse branching in both contralat-

Drug Delivery System

VOL.26 NO.5 SEPTEMBER 2011

通巻第139号／隔月刊

Offprint

Title

Name

Department

Institution

Address

Postal Code City Country

Phone Fax

The Japan Society of Drug Delivery System

Institute of Medical Science
St. Marianna University School of Medicine,
Sugao, Miyamae-ku, Kawasaki, Kanagawa Pref, 216-8512 JAPAN

■ 連載 “DDS研究のための最新機器”

No. 4

生体内リアルタイム共焦点顕微鏡

松本　有[*1~3]，野本貴大[*4]，藤　加珠子[*1]，片岡一則[*1,4]

IVRTCLSM：intravital real-time confocal laser scanning microscopy

DDS開発は高分子化合物のデザインと合成・物性評価・構造解析にはじまり，培養細胞を用いた評価，さらに小動物を用いた評価へ進む．DDSは内包薬剤を保護(ステルス性・安定性)しつつ，標的に送達(選択性・集積性)させ，効率よく薬剤を放出(徐放性・環境応答性)する必要がある．このような一連の高度な機能を空間的・時間的に評価する手法として小動物 *in vivo* イメージングが注目を浴びている．近年，小動物イメージング装置としてPET，SPECT，CT，MRI，可視光，蛍光，発光などを単独あるいは複合的に用いたさまざまな機器が各社から販売されている．これらの装置は，非侵襲的・経時的に個体全体を観察するものであり，すでにDDS研究にとって欠かせないツールとなっているが，空間分解能が低く細胞レベル・細胞内小器官レベルの評価が困難である．

本稿では，筆者が取り組んでいる生体内リアルタイム共焦点顕微鏡(IVRTCLSM：intravital real-time confocal laser scanning microscopy)とDDS研究への応用，今後の展望について述べる．

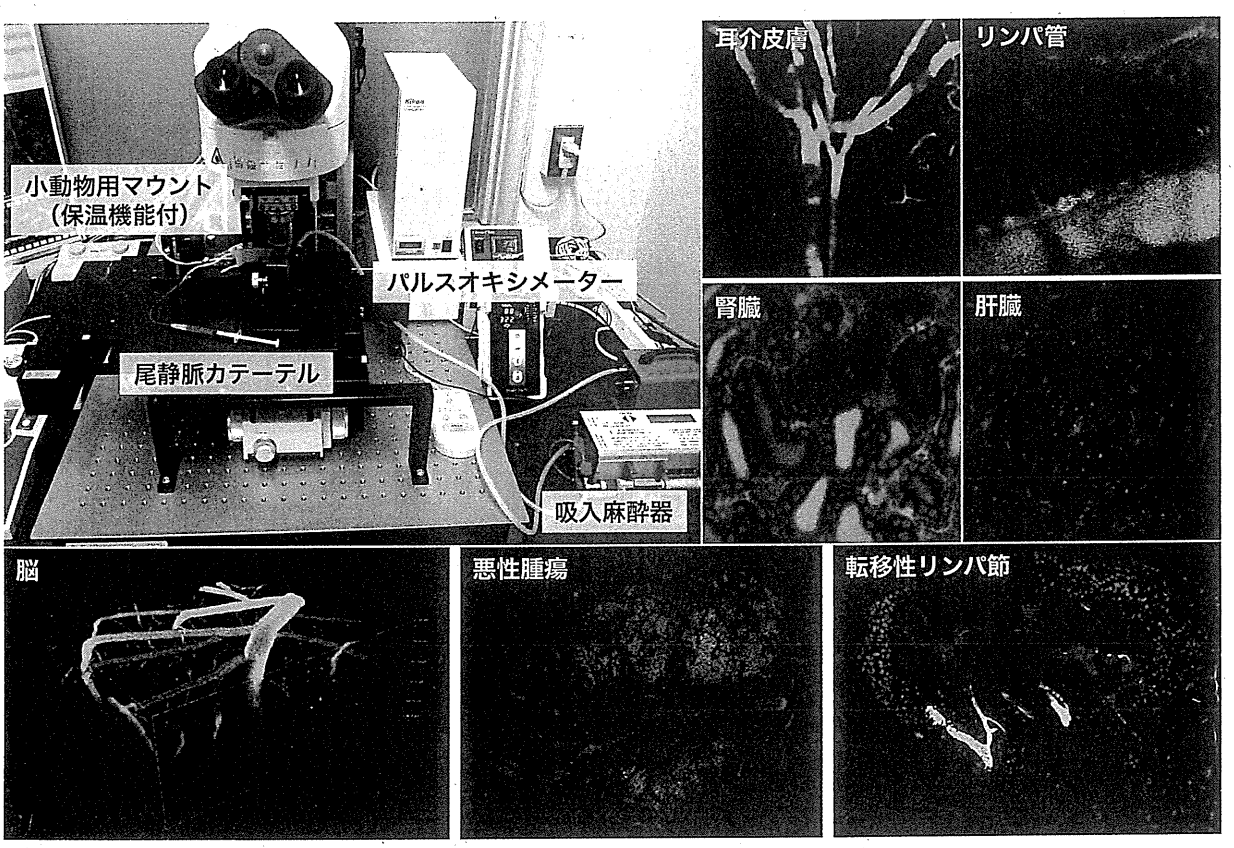

図1　生体内リアルタイム共焦点顕微鏡(IVRTCLSM)

Yu Matsumoto[*1~3]
Takahiro Nomoto[*4]
Kazuko Toh[*1]
Kazunori Kataoka[*1,4]
[*1]Division of Clinical Biotechnology, Center for Disease Biology and Integrative Medicine, Graduate School of Medicine, The University of Tokyo　東京大学大学院医学系研究科附属疾患生命工学センター臨床医工学部門
[*2]Department of Otorhinolaryngology and Head and Neck Surgery, Graduate School of Medicine and Faculty of Medicine, The University of Tokyo　東京大学大学院医学系研究科外科学専攻感覚運動機能講座耳鼻咽喉科学分野
[*3]Department of Otorhinolaryngology and Head and Neck Surgery, Mitsui Memorial Hospital　社会福祉法人三井記念病院耳鼻咽喉科
[*4]Department of Bioengineering, Graduate School of Engineering, The University of Tokyo　東京大学大学院工学系研究科バイオエンジニアリング専攻

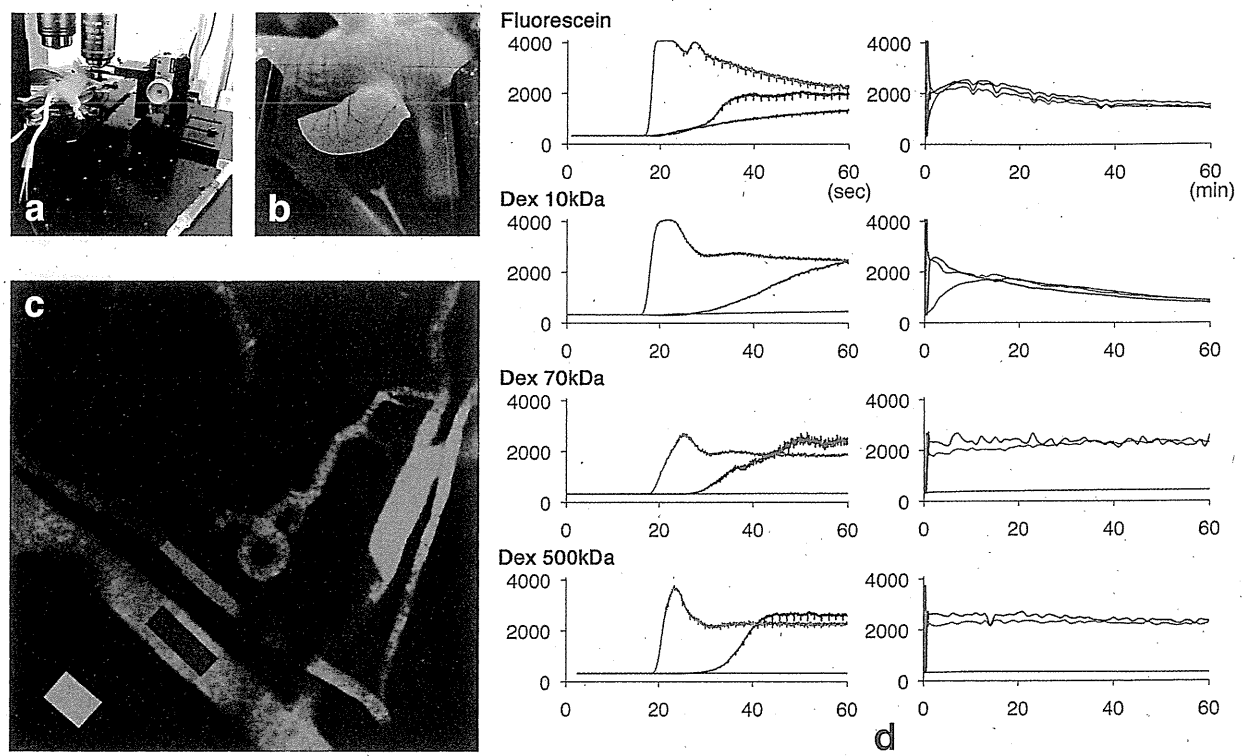

図2　血中滞留性，組織移行性のリアルタイム観察

フルオレセイン(分子量332)またはフルオレセイン標識デキストラン(Dex：平均分子量10 kDa，70 kDa，500 kDa)を尾静脈カテーテル(a)から投与し，耳介皮膚(b)を観察した．得られた画像(c)から動脈，静脈，周囲組織に分けてROIを設定し，平均蛍光強度を経時的にプロットした(d)．フルオレセインは動脈から静脈相に移行すると同時に周囲組織に漏れ出したが，FD 10 kDaは徐々に周囲組織へ漏れ，10～15分をピークに排泄された．FD 70 kDaとFD 500 kDaは血管から漏れることなく60分滞留した．

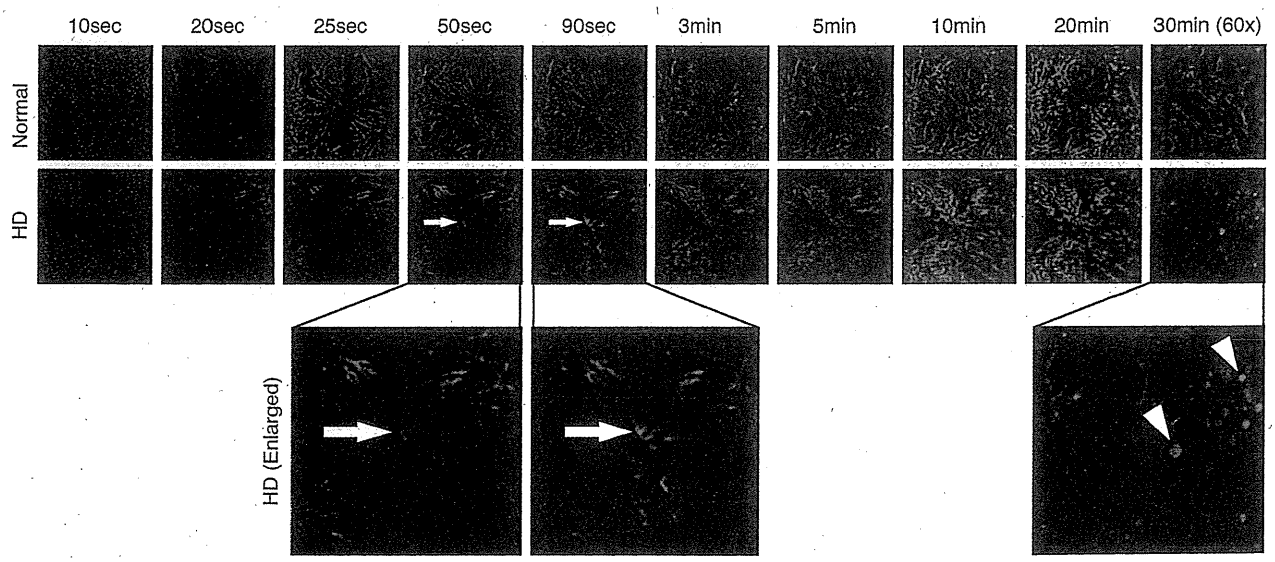

図3　ハイドロダイナミック法がマウス肝臓に及ぼすインパクトの観察

プラスミドDNAをCy5(赤)で標識し，通常法(Normal)およびハイドロダイナミック(HD)法により投与し，肝小葉を観察した．HD法では肝中心静脈からプラスミド遺伝子が逆流し(矢印)，2分間にわたり肝固有動脈と中心静脈が圧平衡を保ち続けた．投与30分後HD法ではNormalにくらべて多くのプラスミド遺伝子が肝細胞核(青)に取り込まれていた(三角)．

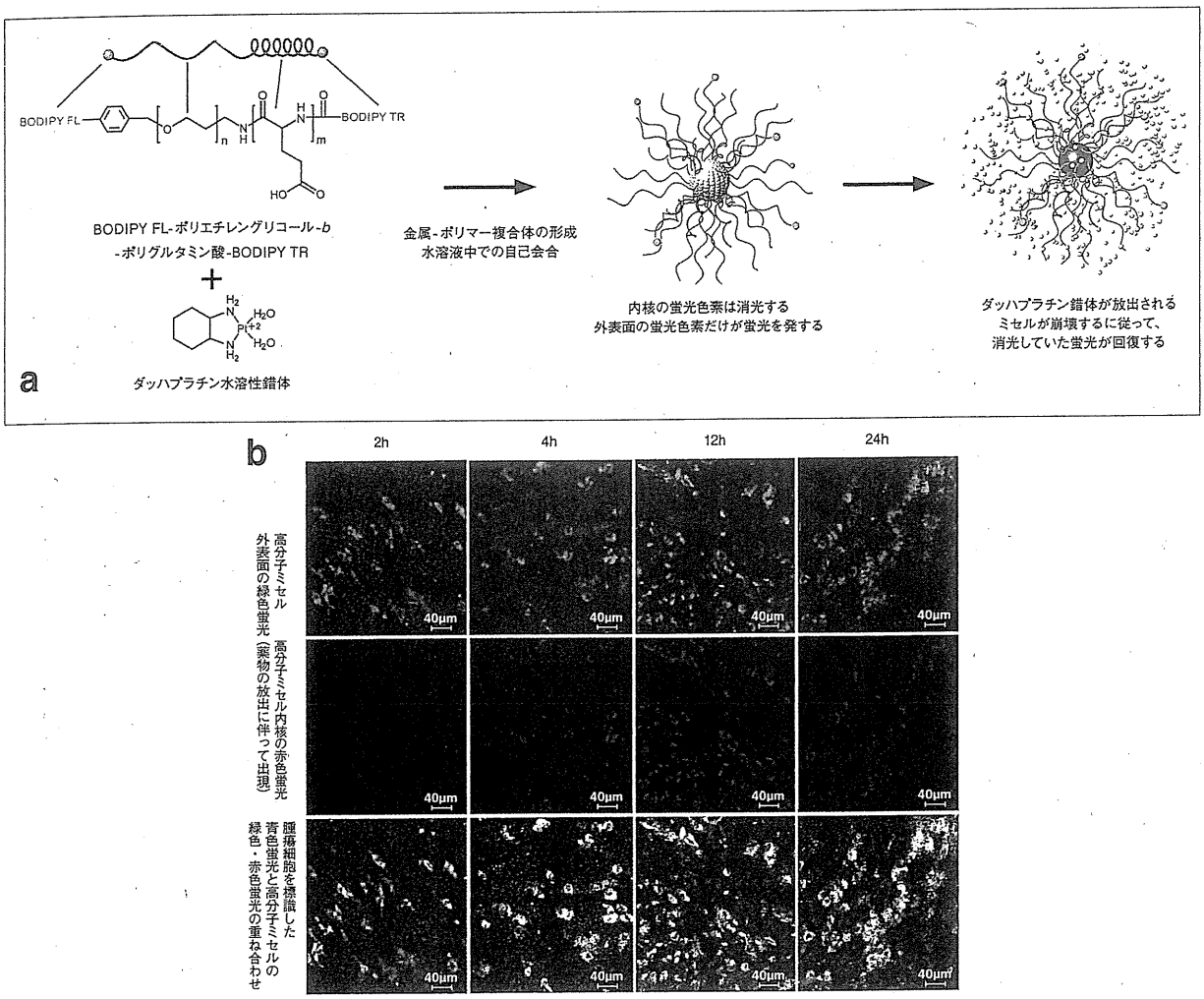

図4　ダッハプラチン内包高分子ミセルの生体内挙動の観察

高分子ミセルの外表面にBODIPY FL(緑)，内核にBODIPY TR(赤)の二つの蛍光色素で標識すると，高分子ミセルが安定な状態では外表面の緑蛍光のみが検出され，内核の赤蛍光は濃度消光を起こす．薬物放出とともに消光状態は解除され，赤蛍光が検出されるようになる(a)．これをヒト大腸がん由来HT29腫瘍モデルマウスに投与し，経時的変化を追跡した．腫瘍細胞をCellMask(青)で標識した．投与直後は高分子ミセルが安定に血中を循環し内包薬剤を放出しなかった[2](Supplementary Video S2参照)．

投与2時間後に腫瘍細胞を標識した青色蛍光とミセルの外表面を標識した緑色蛍光の重なりに示されるように，腫瘍細胞へのミセルの取り込みを認めた．投与4時間後よりミセルが取り込まれた腫瘍細胞において薬剤放出を示す赤色蛍光が経時的に増加し，細胞内で薬剤が徐々に放出される様子が観察された(b)．

生体内リアルタイム共焦点顕微鏡(IVRTCLSM)

IVRTCLSMでは小動物に麻酔をかけて，観察部位を手術によって露出させ，対物レンズの前に固定し，共焦点顕微鏡で観察する．共焦点顕微鏡は深さ方向に分解能を持ち，組織や臓器などの厚い試料から光学的切片画像が得られる．詳しい測定原理については，本誌26-4号「マクロ共焦点顕微鏡を用いた粘膜組織における細胞動態」の稿に譲る．心拍，呼吸，蠕動運動などによる画像のブレを最小限にするため，また血流などの速い動きを捉えるために，高速撮影機能を搭載した装置を用いる．

高速共焦点顕微鏡は，そもそもCaイオンやpHなどの蛍光指示薬を注入した生細胞の動態観察をビデオレート(30 fps)あるいはそれ以上の速さで撮影するために設計されており，マウスが試料台に載ることは考慮されていない．つまり対物レンズの上下の可動域はわずか30 mm程度であり，試料台は培養皿やプレパラートを保持する一般的な物である．小動物を観察するために各研究室で改造を加えている．

筆者の構築したIVRTCLSMはNikon A1Rスキャンユニットと正立顕微鏡ECLIPSE FN1の組み合わせを採用している(図1)．鏡基FN1

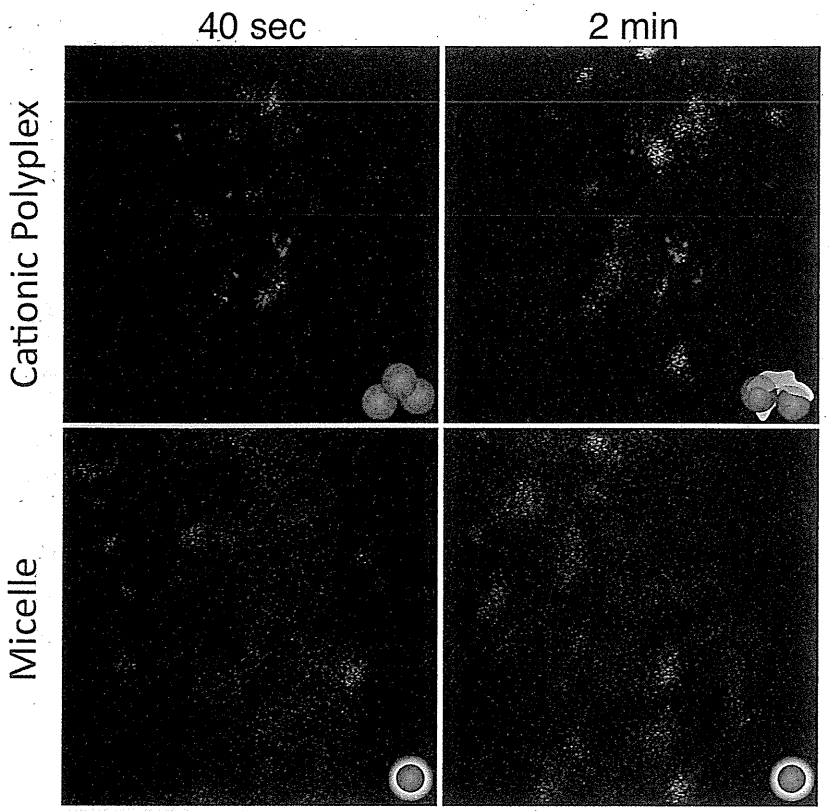

図5　ポリプレックスと高分子ミセルの生体適合性評価

DyLight 488(緑)標識抗 GPIbβ 抗体を静脈投与し血小板を標識した．Cy5(赤)標識プラスミド DNA を用いてポリプレックスと高分子ミセルを調製し，耳介皮膚血管を観察しながら尾静脈カテーテルから投与した．ポリプレックスは投与直後から血中に凝集塊を形成し，数分後にはその凝集塊に血小板が接着した．高分子ミセルは血中に一様に存在し凝集塊形成と血小板との相互作用を認めなかった．

の透過光ユニットを取り外し電動 XY ステージをできるだけ下方に設置することによって小動物を固定する空間を確保した．長時間安定した麻酔を維持するために周辺機器として吸入麻酔器，保温機能付きマウント，パルスオキシメーターなどを揃えている．尾静脈カテーテルを留置すると撮影しながらでも，観察視野を動かすことなく各種試薬の投与が可能である．

応用例

① マウス耳介の真皮深層にある血管を観察しつつ，フルオレセインおよび様々な分子量のフルオレセイン標識デキストランを投与した(図2)．血中滞留性，組織移行性をリアルタイムに追跡し，分子量の違いが薬物動態に及ぼす影響を明確にした[1]．

② マウス肝臓への遺伝子導入として一般的に用いられるハイドロダイナミック法(大量急速静注)のインパクトを肝小葉レベルで観察した(図3)．ハイドロダイナミック法では肝中心静脈からプラスミド遺伝子が逆流し，2分間にわたり肝固有動脈と中心静脈が圧平衡を保ちつづけた．ハイドロダイナミック法では急速な右心房圧上昇により下大静脈の鬱血，肝静脈への逆流が起こり，投与されたプラスミド遺伝子溶液が血液と混合されないまま肝細胞核に送達される様子を確認した[1]．

③ 当研究室で開発したダッハプラチン内包高分子ミセルの生体内挙動について評価した(図4)．投与直後は高分子ミセルが安定に血中を循環し，内包された薬剤を放出しなかった．約12時間後に一部の高分子ミセルは血中から腫瘍細胞に取り込まれ，細胞内で薬剤を放出した．高分子ミセルの腫瘍内取り込みだけでなく腫瘍細胞内での薬剤放出まで経時的に評価することができた[2]．

④ ポリエチレングリコール(PEG)修飾高分子ミセルと PEG の無いポリプレックスの血中滞留性，生体適合性を検討した(図5)．ポリプレックスは投与直後から凝集塊を形成し数分後にはその凝集塊に血小板が接着した．高分子ミセルは凝集塊形成および血小板との相互作用を認めず，血中滞留性が向上した[3]．

DDS 研究・開発での意義と今後の展望

IVRTCLSM は，薬物動態の解析や DDS に付与した高度な機能を評価する手法として有用である．DDS 研究では内包する薬剤を蛍光標識したり，キャリアの高分子側を蛍光標識したり，あるいは標的(がん)細胞に蛍光蛋白質恒常発現株を用いたり，と自由度が高く IVRTCLSM と相性がよい．

DDS は主に癌治療，遺伝子治療を目的としたものであるが，別の観点から考えると蛍光プローブを送達するナノキャリアとしても応用可能である．それまでは培養細胞や組織切片にしかローディング出来なかった蛍光プローブを DDS 技術によって生体の標的細胞で機能させたり，さまざまな蛍光蛋白質を発現させたりすることが出来れば，IVRTCLSM による解析との組み合わせによって生命現象の解析，病態

の解明，多くの疾患診断法の開発などに貢献できる．

機器導入に関連する付帯事項

IVRTCLSMの導入は機器の購入だけでは成しえない．鏡基の改造，小動物用マウントなど特注品の設計と改良，麻酔器などの周辺機器の整備，消耗品の整備に加えて，麻酔科および外科領域の知識と技術が必要である．

日本で購入できる機器メーカーのリスト

高速撮影機能を搭載した市販の共焦点顕微鏡を以下に列挙した．スキャン方式，時間分解能，同時検出可能なチャンネル数などが異なる．

- Nikon社製 A1R (http://www.nikon-instruments.jp/)
- Leica Microsystems社製 TCS SP5 II (http://www.leica-microsystems.com/jp/)
- Carl Zeiss社製 LSM 7 LIVE (http://www.microimaging.zeiss.co.jp/)
- Yokogawa Electric社製 CSU-X1 (http://www.yokogawa.co.jp/)
- Olympus社製 DSU (http://www.olympus.co.jp/)

最後に共焦点内視鏡型顕微鏡について紹介する．小孔から細径プローブを挿入し低侵襲で観察ができる．取り扱いは簡便であるが，感度・撮影速度・チャンネル数に制約がある．

- OptiScan社製 FIVE1 (http://www.optiscan.com/Products/FIVE1.asp)
- VisualSonics社製 Cellvisio LAB (http://www.visualsonics.com/cellviziolab)

本研究は科学技術振興財団(JST)の戦略的基礎研究推進事業(CREST)および日本学術振興会(JSPS)の最先端研究開発支援プログラム(FIRST)の支援により行った．顕微鏡の改造に御尽力いただいた株式会社ニコンインステックに深謝する．

文　献

1) Matsumoto Y, Nomoto T, Cabral H, Matsumoto Y, Watanabe S, Christie RJ, Miyata K, Oba M, Ogura T, Yamasaki Y, Nishiyama N, Yamasoba T, Kataoka K：Direct and instantaneous observation of intravenously injected substances using intravital confocal micro-videography. Biomed Opt Express 1：1209-1216, 2010.
2) Murakami M, Cabral H, Matsumoto Y, Wu S, Kano MR, Yamori T, Nishiyama N, Kataoka K：Improving drug potency and efficacy by nanocarrier-mediated subcellular targeting. Science Translational Medicine 3：64ra2, 2011.
3) Nomoto T, Matsumoto Y, Miyata K, Oba M, Fukushima S, Nishiyama N, Yamasoba T, Kataoka K：In situ quantitative monitoring of polyplexes and polyplex micelles in the blood circulation using intravital real-time confocal laser scanning microscopy. Journal of controlled release 151：104-109, 2011.